AIAA 81-4272

Computationally Efficient, Rotational Nonequilibrium cw Chemical Laser Model

L. H. Sentman*
University of Illinois, Urbana, Ill.
and
W. Rushmore†
Bell Aerospace Textron, Buffalo, N.Y.

The essential fluid dynamic and kinetic phenomena required for a quantitative, computationally efficient, rotational nonequilibrium model of a cw HF chemical laser are identified. It is shown that, in addition to the pumping, collisional deactivation, and rotational relaxation reactions, F-atom wall recombination, the hot pumping reaction, and multiquantum deactivation reactions play a significant role in determining laser performance. Several problems with the HF kinetics package are identified. The effect of various parameters on run time is discussed.

Nomenclature

b_1 = half height of the primary nozzle exit plane
BLT = fraction of primary nozzle filled by the boundary layer
c = speed of light
E_J = rotational energy
f_i = mass fraction of species i
$F(J')$ = Boltzmann rotational distribution function
$G_J^{J'}$ = rotational detailed balance function
h = Planck's constant
I = intensity of lasing transition
J = rotational quantum number
k = Boltzmann's constant
$\bar{K}$ = frequency average of spontaneous emission term, approximated by $\sigma' T^4/\pi$
Le = thickness of mixed flow
Lg = geometric thickness of the flow in the direction of the optical axis
$\dot{m}$ = mass flow rate of the mixed flow
$\dot{m}_p$ = mass flow rate remaining in the primary stream
$\dot{m}_s$ = mass flow rate remaining in the secondary stream
$\mathfrak{M}$ = dipole moment
n_i = mole mass ratio of species i
N_A = Avogadro's number
P = pressure of mixed flow
$P_J^{J'}$ = rotational transition probability
$P^M_{v',J';v,J}$ = transition probability for the lasing species state change $v',J' \rightarrow v,J$ due to collision with species M
r_0, r_L = mirror reflectivities
$\mathfrak{R}$ = universal gas constant
T = temperature of mixed flow
u = velocity of mixed flow
v = vibrational quantum number
W_i = molecular weight of species i
x = coordinate in flow direction
Z = bimolecular collision frequency $= \sigma^2 N_A (8\pi kT/\mu)^{1/2}$
z = coordinate in the direction of the lasing axis
α = gain
δ_1 = thickness of the mixing layer
δ_{BL} = thickness of the boundary layer in the nozzle exit plane
θ_r = rotational temperature of lasing species
μ = reduced mass of colliding molecules
ρ = density of mixed flow
σ' = Stefan-Boltzmann constant
ϕ = line shape profile
χ = rate of change of species mole mass ratio due to stimulated emission of radiation
ω_{ij} = energy difference of transition ij in cm^{-1}

Superscript

M = species M

Subscripts

c = vibrational-rotational relaxation
L = lower level of lasing transition
0 = value at nozzle exit plane
p = primary stream
r = rotational relaxation
s = secondary stream
U = upper level of lasing transition

Received July 10, 1980; revision received March 20, 1981.

*Professor, Aeronautical and Astronautical Engineering. Member AIAA.

†Research Scientist, High Energy Laser Technology. Member AIAA.

I. Introduction

THE performance of a cw chemical laser is determined by the nonlinear interactions which occur between the fluid dynamics, chemical kinetics, and optical resonator. Of all of the phenomena that occur in chemical lasers, rotational nonequilibrium is the dominant mechanism responsible for the power spectral output. The significant effects of rotational nonequilibrium on the performance of chemical lasers have been described in the HF cw case by Sentman[1] and in the pulsed case by Hough and Kerber.[2] The DF cw case has been treated by Hall[3] and the HF single-line amplifier by Skifstad.[4] The agreement between these calculations and the experimental data showed that when rotational nonequilibrium is included in the model, several J transitions within a given vibrational band lase simultaneously, most of the power is contained in those J transitions which are preferentially populated by the pumping reaction, and the power is decreased by 20-30% from the rotational equilibrium value. All of these studies employed a Fabry-Perot model for the optical cavity, whereas high-energy lasers usually extract

power with an unstable resonator. The effect of the optical model on cw laser performance was examined by Sentman.[5] Calculations were performed for both rotational equilibrium and nonequilibrium cases for a confocal unstable resonator with 50% geometric outcoupling. For the rotational equilibrium case, the solution resulted in most of the power being contained in one line. For the rotational nonequilibrium case, the power is distributed over eleven lines, and the Fabry-Perot and unstable resonator power spectral distributions are almost identical, the major difference being that all lines whose saturated gain region does not extend into the central portion of the unstable resonator are cut off. For the rotational nonequilibrium case, fluctuations in cw power were shown to occur on lines whose saturated gain zone does not fill the unstable resonator. The amplitude of the fluctuation was determined by the fraction of the resonator filled by the saturated gain zone of the oscillating line, and the frequency of the fluctuation was determined by the location of the intensity peak of the oscillating line.

These studies have demonstrated that:

1) Rotational nonequilibrium plays a major role in determining the power spectral performance of the laser. This phenomenon must be included in any model, Fabry-Perot or unstable resonator, which is to predict the power spectral performance of the laser.

2) Rotational equilibrium models overpredict the total power and maximum intensity.

3) For rotational nonequilibrium, the Fabry-Perot and unstable resonator power spectral distributions are nearly identical.

4) Rotational nonequilibrium is the mechanism responsible for a nonlinear coupling which may occur between the saturated gain and the resonator geometry resulting in large-amplitude fluctuations on a given line.

Since the computation time for a computer model of a chemical laser depends upon N^2, where N is the number of dependent variables, the necessity of including rotational nonequilibrium in the model will result in a significant increase in run time because the number of dependent variables will increase from about 30 to 80, or more. The main thrust of the present work was to modify the qualitative, but computationally efficient, rotational nonequilibrium cw chemical laser model developed by Sentman[1,5] so that it would give quantitative predictions of the power spectral performance of the laser.

In Sec. II, the approach used and the kinetic fluid dynamic model which has evolved is described; in Sec. III, the validity of the model is demonstrated through detailed comparisons with the results from the sophisticated, rotational equilibrium chemical laser model Blaze II[6] for two different cases. Some comments on run time are given and several problems with the HF rate package that were discovered during this work are discussed.

II. Kinetic Fluid Dynamic Model

For computational efficiency, the number of dependent variables must be kept to a minimum. Based on experience with an earlier model,[1] the approach used in this study was to include the essential chemical kinetics—the pumping reactions, major deactivation reactions, and rotational relaxation reactions—and to include the fluid dynamic effects of mixing by inputting the pressure, temperature, velocity, mass flow rate remaining in the primary, mass flow rate remaining in the secondary, and the length of the active media as functions of x which are obtained from one of the available quasi-2-D, 2-D, or 3-D fluid dynamic, rotational equilibrium, chemical kinetic laser models.[6-8] This approach was motivated by the fact that changes in chemical kinetics, which significantly affect the power spectral performance, in most cases, have only a minor effect on the flowfield in which the kinetics takes place. Thus, the fluid dynamics provide the environment in which the kinetics occur.

Since the present model, denoted MNORO, will reproduce the rotational equilibrium results when it is run using a value of the rotational relaxation rate constant which is 10^5 times its measured value, the model has evolved from detailed comparisons with the rotational equilibrium Blaze II model[6] for two different cases: an arc-driven HF power spectral experiment[9] and the CL XI lasing lines experiment.[10] These two cases were chosen because, in addition to providing power spectral data, and in the CL XI case, intensity distributions on each line, they represent two extremes of fluid dynamic mixing; analysis of the arc-driven case shows that the mixing rates are slower than the CL XI nozzle which uses a gasdynamic trip mechanism. This variance between the two cases should insure that the polynomial fits used for the fluid variables are capable of handling any profiles likely to be encountered.

For purposes of developing the kinetic fluid dynamic model, the optical cavity was modeled as a Fabry-Perot resonator. The geometry is shown in Fig. 1. When rotational nonequilibrium is included in the model, several J transitions within each vibrational band lase simultaneously with the dominant ones being determined by the J dependence of the pumping reaction.[1] Because of this, the treatment of rotational nonequilibrium effects is facilitated by using a more exact treatment of the radiation field than that afforded by the constant gain approximation. The description of the radiation field employed is that developed in Ref. 1, in which the radiative transfer equations are solved for a Fabry-Perot cavity to obtain an equation for the average intensity, I, as a function of the gain, α. With this expression for I, the χ term

$$I_{\nu_{UL}} = 4\bar{K} r_0 r_L \alpha_{\nu_{UL}} Le / (1 - r_0 r_L - 2 r_0 r_L \alpha_{\nu_{UL}} Le) \tag{1}$$

in the species equations for n_U and n_L is given by

$$\chi_{UL} = \alpha_{\nu_{UL}} I_{\nu_{UL}} / h N_A \nu_{UL} \tag{2}$$

The retention of the spontaneous emission term, S_ν, in the radiative transfer equations resulted in an explicit expression for the intensity in terms of the species variables. With this result, the χ terms are simply nonlinear terms on the right-hand sides of the species equations. Thresholds and cutoffs are obtained as part of the solution of the differential equations for the species variables.

The original rotational nonequilibrium model[1] was a two-level, premixed model in which the pumping reaction did not conserve mass and deactivation was included by collision with a generic species. To obtain quantitative predictions, the correct pumping and collisional deactivation reactions in-

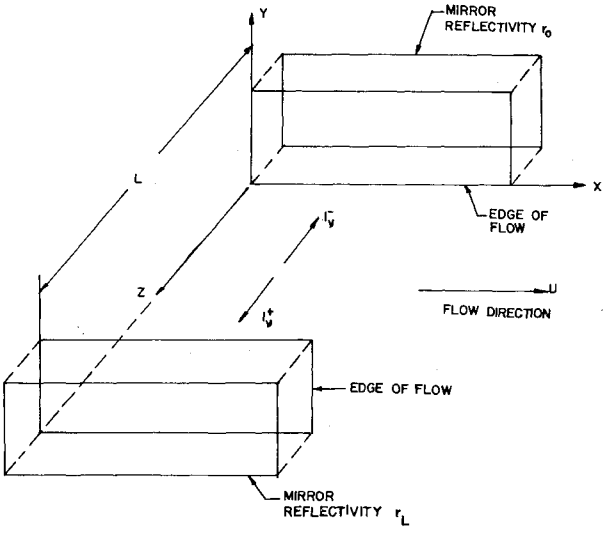

Fig. 1 Flow and optical geometry.

volving the primary deactivators HF, F, H, and H_2 have been included. The model as it has developed to date comprises the following reaction set.

Pumping reactions:

$$F + H_2 \rightarrow HF(1,J) + H \tag{3}$$

$$F + H_2 \rightarrow HF(2,J') + H \tag{4}$$

$$F + H_2 \rightarrow HF(3) + H \tag{5}$$

$$F_2 + H \rightarrow HF(3) + F \tag{6}$$

Collisional deactivation reactions:

$$HF(2,J') + M \rightleftarrows HF(1,J) + M \tag{7}$$

$$HF(1,J) + M \rightleftarrows HF(0) + M \tag{8}$$

$$HF(3) + M \rightleftarrows HF(2,J') + M \tag{9}$$

where M = HF, F, H, and H_2.

$$HF(2,J) + M \rightleftarrows HF(0) + M \tag{10}$$

$$HF(3) + M \rightleftarrows HF(1,J) + M \tag{11}$$

$$HF(3) + M \rightleftarrows HF(0) + M \tag{12}$$

where M = HF, F, and H.

Rotational relaxation reactions:

$$HF(2,J') + M \rightleftarrows HF(2,J) + M \tag{13}$$

$$HF(1,J) + M \rightleftarrows HF(1,J'') + M \tag{14}$$

where M = HF, F, H, H_2, F_2, He, and Ar.

The species denoted by Ar is included to take account of any other combustion or dissociation products that may be present in the mixture and which would contribute to the rotational relaxation but not the collisional deactivation of the lasing species.

The above model, while retaining the key chemical kinetics, is quite concise compared to the kinetic models employed in codes such as Blaze II[6] or Lamp.[7] As shown in Sec. III, to duplicate the species profiles calculated by Blaze II, it was necessary to include reactions (5), (6), (8), and (9) in the model. As will be shown later, the addition of the multiquantum deactivation reactions (10-12) has a significant effect on the power and the length of the lasing zone.

The χ_{chem} terms for the above reactions are developed in Ref. 11. The global rate constants are input in the usual way as

$$k = AT^{-N}\exp(-B/RT) \tag{15}$$

where A, N, and B are input constants. For the J-dependent reactions, the rate constants are now J-dependent. For the pumping reactions,

$$k_{pvJ} = k_p^v f^v(J) \tag{16}$$

where k_p^v are the global forward reaction rates that have been determined experimentally as a function of temperature and which are used in the rotational equilibrium models; $f^v(J)$ is the normalized distribution over the rotational states of each v level ($\Sigma_J f^v(J) = 1$) which is obtained from experiment. For HF and DF, the data of Polanyi and Woodall[12] are used for $f^v(J)$. The pumping reactions are assumed to be one-way reactions.

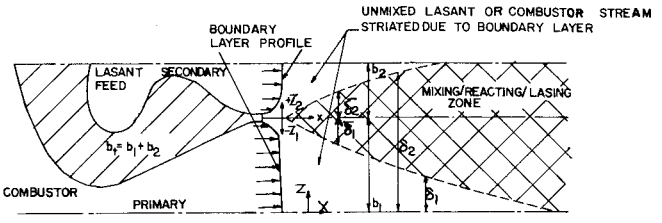

Fig. 2 Schematic of the mixing region.

For the *V-R* collisional deactivation reactions, the detailed rate constants are expressed as

$$k^M_{v',J';v,J} = ZC_1 T^{-(N+1)} \exp\{-C_2[hc\omega_{v',v}/kT + (E_{J'} - E_J)/kT]\} \tag{17}$$

C_1 and C_2 are input constants determined by requiring that the following relation be satisfied[1]:

$$k^M_{v',v} = \sum_J \sum_{J'} F(J') k^M_{v',J';v,J} \tag{18}$$

where the global rate constant $k^M_{v',v}$, which is determined experimentally, is expressed by Eq. (15).

The rotational relaxation rate constants are expressed[13] as

$$k^M_r = E_{M_r} k^{\text{HF}}_r \tag{19}$$

where

$$k^{\text{HF}}_r = Z_r C_{1r} \exp[-C_{2r}(E_{J'} - E_J)/kT] \tag{20}$$

C_{1r} and C_{2r} are input constants determined from experiment[14,15] and E_{M_r} is the rotational relaxation efficiency of species M compared to HF.

To keep the number of dependent variables to a minimum, $P(x)$, $T(x)$, $u(x)$, $\dot{m}_p(x)$, $\dot{m}_s(x)$, and Le/Lg are input as functions of x from a detailed rotational equilibrium model such as Blaze II. These functions are input as polynomials in x, where the coefficients are determined by a least-squares fit to the Blaze II profiles. Experience has shown that P, T, and u require ninth-order polynomials, $\dot{m}_p$ and $\dot{m}_s$ require a quadratic in $\sqrt{x}$, and Le/Lg requires $\sqrt{x}$ times a quadratic in $x^{1/4}$. The coefficients of these polynomials are input data.

A schematic of a typical mixing region is shown in Fig. 2. From Ref. 16, the mixing term which appears in the species equation is given by

$$M_{ni} = \frac{1}{\dot{m}}\left[(n_i - n_{is0})\frac{d\dot{m}_s}{dx} + (n_i - n_{ip0})\frac{d\dot{m}_p}{dx}\right] \tag{21}$$

For the products of reaction, $n_{is0} = n_{ip0} = 0$; for reactants from the primary stream, $n_{is0} = 0$; for reactants from the secondary stream, $n_{ip0} = 0$. The mass flow rate of the mixed stream is given by

$$\dot{m} = \dot{m}_{p0} - \dot{m}_p + \dot{m}_{s0} - \dot{m}_s \tag{22}$$

The resulting species equations are:

$$\frac{dn_{\text{HF}}(1,J)}{dx} = \frac{\rho}{u}\Big\{k^1_p f^1(J) n_{\text{F}} n_{\text{H}_2} + \sum_M \Big\{n_M Z^M_c \Big[\sum_{J'=0}^{J} n_{\text{HF}}(2,J') P^M_{2,J;1,J'} G^J_{J'} + \sum_{J'=J+1}^{J_M} n_{\text{HF}}(2,J') P^M_{2,J';1,J} - \exp(-hc\omega_{21}/kT)$$

$$\times\left(\sum_{J'=0}^{J} P^{M}_{2,J;1,J'}+\sum_{J'=J+1}^{J_M} P^{M}_{2,J';1,J}G^{J'}_{J}\right)n_{\mathrm{HF}}(1,J)\Big]\Big\}$$

$$-Z^{\mathrm{HF}}_{r}\left(n_{\mathrm{HF}}+\sum_{M} n_M E_{Mr}\right)\Big[n_{\mathrm{HF}}(1,J)$$

$$\times\left(\sum_{J''=0}^{J-1} P^{J}_{J''}+\sum_{J''=J+1}^{J_M} P^{J''}_{J}G^{J''}_{J}\right)$$

$$-\sum_{J''=0}^{J-1} P^{J}_{J''}G^{J}_{J''}n_{\mathrm{HF}}(1,J'')-\sum_{J''=J+1}^{J_M} P^{J''}_{J}n_{\mathrm{HF}}(1,J'')\Big]$$

$$-[n_{\mathrm{HF}}(1,J)-\exp(-hc\omega_{10}/kT)F(J)n_{\mathrm{HF}}(0)]\sum_{M} n_M k^{M}_{10}$$

$$+n_{\mathrm{HF}}(3)F(J)\sum_{M} n_M k^{M}_{31}\Big\}+\frac{1}{\rho u}[\chi(1,J,-1)$$

$$+\chi(1,J,1)]+\frac{1}{\dot m}\left[\frac{\mathrm{d}\dot m_p}{\mathrm{d}x}+\frac{\mathrm{d}\dot m_s}{\mathrm{d}x}\right]n_{\mathrm{HF}}(1,J) \tag{23}$$

$$\frac{\mathrm{d}n_{\mathrm{HF}}(2,J')}{\mathrm{d}x}=\frac{\rho}{u}\Big\{k_p^2 f^2(J')n_{\mathrm{F}}n_{\mathrm{H_2}}$$

$$-\sum_{M}\Big\{n_M Z^{M}_{c}\Big[n_{\mathrm{HF}}(2,J')\Big(\sum_{J=0}^{J'} P^{M}_{2,J';1,J}$$

$$+\sum_{J=J'+1}^{J_M} P^{M}_{2,J;1,J'}G^{J}_{J'}\Big)-\exp(-hc\omega_{21}/kT)$$

$$\times\Big(\sum_{J=0}^{J'} n_{\mathrm{HF}}(1,J)P^{M}_{2,J';1,J}G^{J'}_{J}+\sum_{J=J'+1}^{J_M} n_{\mathrm{HF}}(1,J)P^{M}_{2,J;1,J'}\Big)\Big]\Big\}$$

$$-Z^{\mathrm{HF}}_{r}\left(n_{\mathrm{HF}}+\sum_{M} n_M E_{Mr}\right)$$

$$\times\Big[n_{\mathrm{HF}}(2,J')\Big(\sum_{J=0}^{J'-1} P^{J'}_{J}+\sum_{J=J'+1}^{J_M} P^{J}_{J'}G^{J}_{J'}\Big)$$

$$-\sum_{J=0}^{J'-1} P^{J'}_{J}G^{J'}_{J}n_{\mathrm{HF}}(2,J)-\sum_{J=J'+1}^{J_M} P^{J}_{J'}n_{\mathrm{HF}}(2,J)\Big]$$

$$-n_{\mathrm{HF}}(2,J')\sum_{M} n_M k^{M}_{20}+[n_{\mathrm{HF}}(3)F(J')-n_{\mathrm{HF}}(2,J')$$

$$\times\exp(-hc\omega_{32}/kT)]\sum_{M} n_M k^{M}_{32}\Big\}$$

$$-\frac{1}{\rho u}[\chi(1,J'+1,-1)+\chi(1,J'-1,1)]$$

$$+\frac{1}{\dot m}\left[\frac{\mathrm{d}\dot m_p}{\mathrm{d}x}+\frac{\mathrm{d}\dot m_s}{\mathrm{d}x}\right]n_{\mathrm{HF}}(2,J') \tag{24}$$

$$\frac{\mathrm{d}n_{\mathrm{F}}}{\mathrm{d}x}=-\frac{\rho}{u}\Big\{k_{PT}n_{\mathrm{F}}n_{\mathrm{H_2}}-k_{PHT}n_{\mathrm{H}}n_{\mathrm{F_2}}\Big\}$$

$$+\frac{1}{\dot m}\left[n_{\mathrm{F}}\frac{\mathrm{d}\dot m_s}{\mathrm{d}x}+(n_{\mathrm{F}}-n_{\mathrm{F}0})\frac{\mathrm{d}\dot m_p}{\mathrm{d}x}\right] \tag{25}$$

$$\frac{\mathrm{d}n_{\mathrm{H_2}}}{\mathrm{d}x}=-\frac{\rho}{u}k_{PT}n_{\mathrm{F}}n_{\mathrm{H_2}}+\frac{1}{\dot m}\Big[(n_{\mathrm{H_2}}-n_{\mathrm{H_{2_0}}})$$

$$\times\frac{\mathrm{d}\dot m_s}{\mathrm{d}x}+n_{\mathrm{H_2}}\frac{\mathrm{d}\dot m_p}{\mathrm{d}x}\Big] \tag{26}$$

$$\frac{\mathrm{d}n_{\mathrm{H}}}{\mathrm{d}x}=\frac{\rho}{u}[k_{PT}n_{\mathrm{F}}n_{\mathrm{H_2}}-k_{PHT}n_{\mathrm{H}}n_{\mathrm{F_2}}]+\frac{1}{\dot m}\left[\frac{\mathrm{d}\dot m_s}{\mathrm{d}x}+\frac{\mathrm{d}\dot m_p}{\mathrm{d}x}\right]n_{\mathrm{H}} \tag{27}$$

$$\frac{\mathrm{d}n_{\mathrm{He}}}{\mathrm{d}x}=\frac{1}{\dot m}\left[(n_{\mathrm{He}}-n_{\mathrm{He}_{s0}})\frac{\mathrm{d}\dot m_s}{\mathrm{d}x}+(n_{\mathrm{He}}-n_{\mathrm{He}_{p0}})\frac{\mathrm{d}\dot m_p}{\mathrm{d}x}\right] \tag{28}$$

$$\frac{\mathrm{d}n_{\mathrm{Ar}}}{\mathrm{d}x}=\frac{1}{\dot m}\left[(n_{\mathrm{Ar}}-n_{\mathrm{Ar}_{s0}})\frac{\mathrm{d}\dot m_s}{\mathrm{d}x}+(n_{\mathrm{Ar}}-n_{\mathrm{Ar}_{p0}})\frac{\mathrm{d}\dot m_p}{\mathrm{d}x}\right] \tag{29}$$

$$\frac{\mathrm{d}n_{\mathrm{F_2}}}{\mathrm{d}x}=-\frac{\rho}{u}k_{PHT}n_{\mathrm{H}}n_{\mathrm{F_2}}+\frac{1}{\dot m}\Big[(n_{\mathrm{F_2}}-n_{\mathrm{F_{2s0}}})\frac{\mathrm{d}\dot m_s}{\mathrm{d}x}$$

$$+(n_{\mathrm{F_2}}-n_{\mathrm{F_{2p0}}})\frac{\mathrm{d}\dot m_p}{\mathrm{d}x}\Big] \tag{30}$$

$$\frac{\mathrm{d}n_{\mathrm{HF}}(0)}{\mathrm{d}x}=\frac{\rho}{u}\Big\{[n_{\mathrm{HF}}(1)-\exp(-hc\omega_{10}/kT)n_{\mathrm{HF}}(0)]$$

$$\times\sum_{M} n_M k^{M}_{10}+n_{\mathrm{HF}}(2)\sum_{M} n_M k^{M}_{20}+n_{\mathrm{HF}}(3)\sum_{M} n_M k^{M}_{30}\Big\}$$

$$+\frac{1}{\dot m}\left[\frac{\mathrm{d}\dot m_s}{\mathrm{d}x}+\frac{\mathrm{d}\dot m_p}{\mathrm{d}x}\right]n_{\mathrm{HF}}(0) \tag{31}$$

$$\frac{\mathrm{d}n_{\mathrm{HF}}(3)}{\mathrm{d}x}=\frac{\rho}{u}\Big\{n_{\mathrm{F}}n_{\mathrm{H_2}}k_p^3-[n_{\mathrm{HF}}(3)-n_{\mathrm{HF}}(2)$$

$$\times\exp(-hc\omega_{32}/kT)]\sum_{M} n_M k^{M}_{32}+n_{\mathrm{H}}n_{\mathrm{F_2}}k^{3}_{PH}-n_{\mathrm{HF}}(3)$$

$$\times\sum_{M} n_M[k^{M}_{30}+k^{M}_{31}]\Big\}+\frac{1}{\dot m}\left[\frac{\mathrm{d}\dot m_s}{\mathrm{d}x}+\frac{\mathrm{d}\dot m_p}{\mathrm{d}x}\right]n_{\mathrm{HF}}(3) \tag{32}$$

where k_{PT} is the sum of k_p^v over $v=1$-3, $k_{PHT}=k^3_{PH}$, and k^3_{PH} is the sum of k^v_{PH} over $v=3$-6. With $J_M=20$, there are 50 differential equations for the mole mass ratios of the various species in the mixture. The initial values of the mole mass ratios of the species are calculated from the initial flow rates of the species in the primary and secondary streams.

$$n_{ip0}=\dot m_{ip0}/\dot m_{p0}W_i \tag{33}$$

$$n_{is0}=\dot m_{is0}/\dot m_{s0}W_i \tag{34}$$

In some cases, F-atom recombination at the wall is important. This effect is included by varying the F-atom concentration in the primary stream from zero at the wall to its value in the core of the primary flow. This results in a variation of n_{Fp0}, the value of n_F at the edge of the mixing layer which appears in the mixing terms, with x. The boundary-layer profile is used to provide the variation of n_F from the wall to the core. The mole mass ratio is related to the species mass fraction by

$$n_{i_0}(z)=f_i/W_i \tag{35}$$

The value of z depends upon the value of x, and the thickness of the mixing layer $z=\bar\delta_l(x)$ at that value of x. Thus,

$$n_{\mathrm{F}_0}=n_{\mathrm{F_{wall}}}+[n_{\mathrm{F_{core}}}-n_{\mathrm{F_{wall}}}]\left[\frac{\bar\delta_l(x)}{\delta_{BL}}\right]^{3/2} \tag{36}$$

$$n_{\mathrm{F_{2_0}}}=n_{\mathrm{F_{2wall}}}+[n_{\mathrm{F_{2core}}}-n_{\mathrm{F_{2wall}}}]\left[\frac{\bar\delta_l(x)}{\delta_{BL}}\right]^{3/2} \tag{37}$$

Table 1 Blaze II CL XI results when various bands are allowed to lase (relative powers and lasing zone lengths are shown)

Bands lasing	Lasing zone length	Total power	$\frac{P_{10}}{P_T}$ $\left(\frac{P_{10}}{P_T}\right)_{\text{all bands}}$	$\frac{P_{21}}{P_T}$ $\left(\frac{P_{21}}{P_T}\right)_{\text{all bands}}$	$\frac{P_{32}}{P_T}$ $\left(\frac{P_{32}}{P_T}\right)_{\text{all bands}}$	$\frac{P_{43}}{P_T}$	$\frac{P_{54}}{P_T}$	$\frac{P_{65}}{P_T}$	$\frac{P_{76}}{P_T}$
All bands	1	1	0.417	0.422	0.113	0.0019	0.025	0.0198	0
32, 21, 10	1	0.956	0.436 (0.417)	0.443 (0.423)	0.122 (0.117)				
21, 10	0.909	0.740	0.518 (0.384)	0.482 (0.356)					

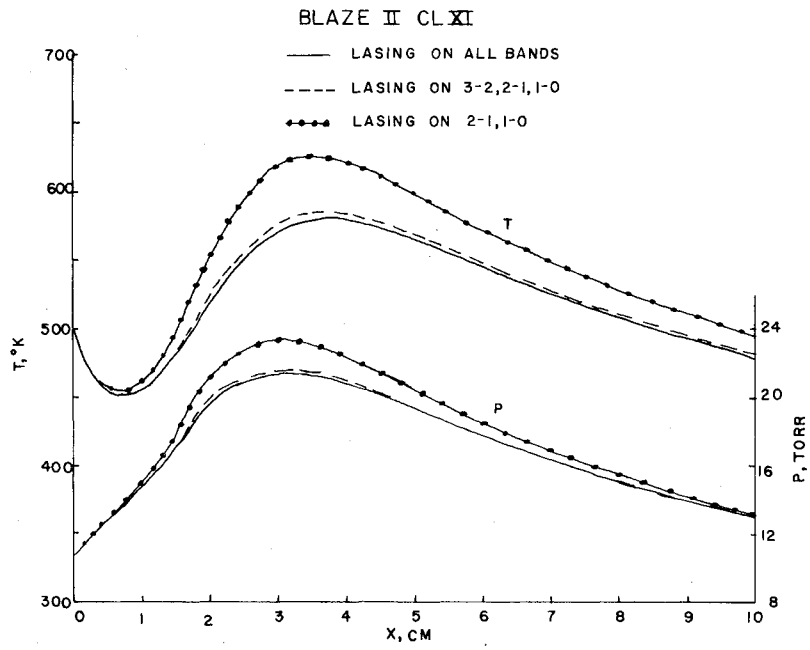

Fig. 3 Blaze II CL XI temperature and pressure profiles.

Since the number of F atoms must be conserved, $n_{\text{F}_{2\text{wall}}}$ is related to $n_{\text{F}_{\text{wall}}}$ by

$$n_{\text{F}_{2\text{wall}}} = \tfrac{1}{2} n_{\text{F}_{\text{core}}} + n_{\text{F}_{2\text{core}}} - \tfrac{1}{2} n_{\text{F}_{\text{wall}}} \tag{38}$$

where the ½ occurs because $W_{\text{F}_2} = 2W_{\text{F}}$. The boundary-layer profile is input from Blaze II as

$$\delta_l(x)/b_l = ax^{1/4} + bx^{1/2} \tag{39}$$

where $\delta_{BL} = BLT \times b_l$ and a and b are curve-fit constants determined by fitting Eq. (39) to the Blaze II data.

The final element of the model is the inclusion of the effect of lasing on the 1:0 band. This was necessary to obtain quantitative agreement with the Blaze II results. Since the present model is a two-level model, the effect of lasing on the 1:0 band was included as a rate constant k^{10}_{rad}, which was determined from the Blaze II value of $\chi^{10}_{\text{rad}}(x)$ by setting

$$\chi^{10}_{\text{rad}} = k^{10}_{\text{rad}} \rho^2 n_{\text{HF}} n_{\text{HF}}(1) \tag{40}$$

which simulates the depopulation of HF(1) by lasing as a collisional deactivation by HF. From Eq. (40), $k^{10}_{\text{rad}}(x)$ is obtained and input as a function of x in the program. The rate constant for the deactivation of HF(1) by HF is then written as

$$k_{10} = k^{\text{HF}}_{10} + k^{10}_{\text{rad}} \tag{41}$$

and the effect of lasing on the depopulation of HF(1) is taken into account in the collisional deactivation reaction.

The gain is given by

$$\alpha(v,J,m) = \rho h N_A \omega_{UL} \phi(\omega_{UL}) B_{LU} [(g_L/g_U) n_U - n_L] \tag{42}$$

where for a Doppler profile

$$\omega_{UL}\phi_D = c\left(\frac{W_L}{2\pi\mathfrak{R}}\right)^{1/2} T^{-1/2} \tag{43}$$

W_L is the molecular weight of the lasing species,

$$B_{LU} = \frac{4\pi^3}{3h^2 c} |\mathfrak{M}|^2 \left(\frac{2J+1+m}{2J+1}\right) \tag{44}$$

$$g_L = 2J+1, \quad g_U = 2J+1+2m \tag{45}$$

and $m = -1$ for the P branch and $m = +1$ for the R branch. For a Voight profile,

$$\phi_{\text{Voight}} = \phi_D K(0,y) \tag{46}$$

where $K(0,y)$ is given in Ref. 6. The power in each transition is given by

$$P(x,v,J,m) = \frac{hN_A c\omega_{21}}{F_{JM}} \int_0^x A_{mT} \chi(v,J,m)\,dx \tag{47}$$

where $A_{mT} = \dot{m}/\rho u$, and

$$F_{Jm} = \omega_{21}/\omega_{UL} = \{1 + [m(2J+1+m)\theta_r k/hc\omega_{21}]\}^{-1} \tag{48}$$

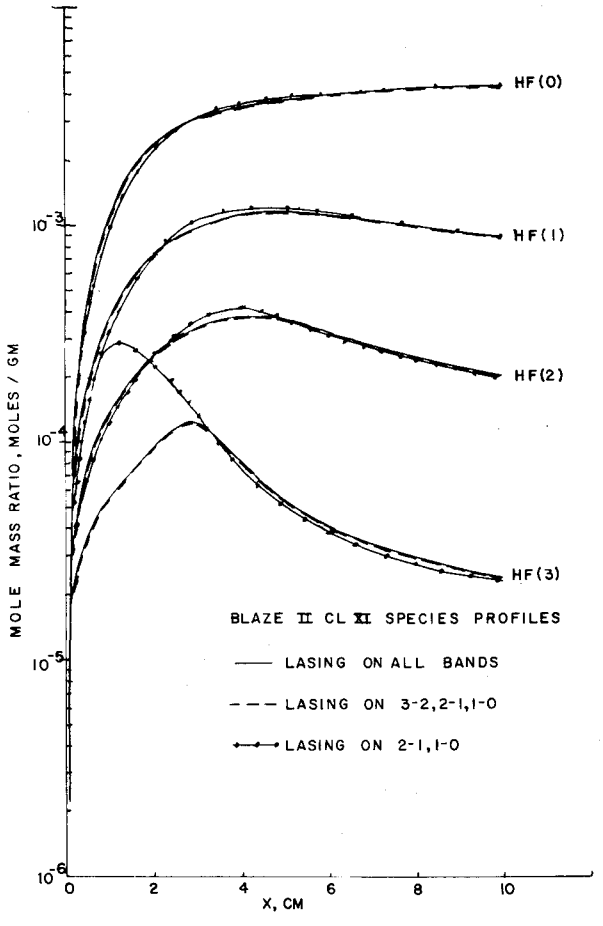

Fig. 4 Blaze II CL XI HF(v) profiles.

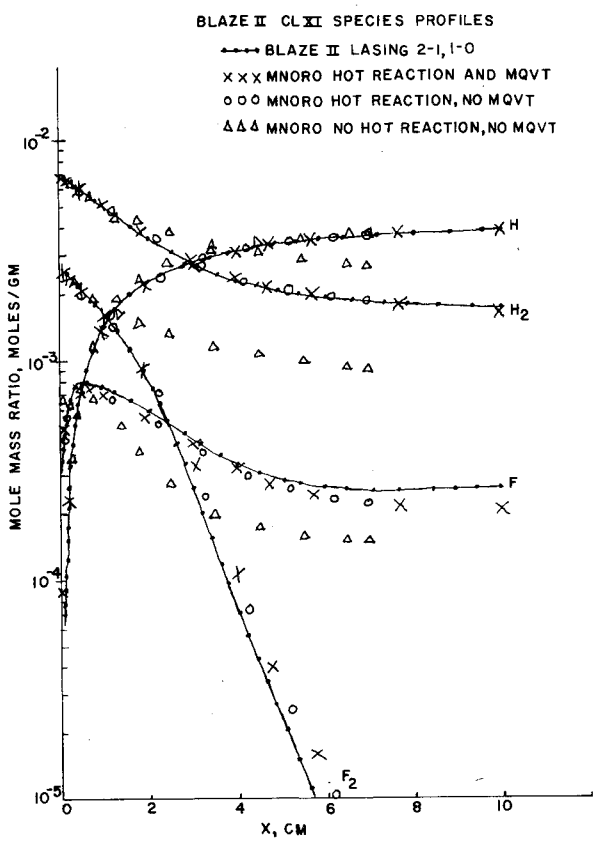

Fig. 5 Comparison of Blaze II and MNORO rotational equilibrium H, F, H_2, and F_2 profiles for the CL XI showing the effect of the hot reaction and multiquantum VT deactivation (MQVT).

The density ρ is given by

$$\rho = PW/\Re T \tag{49}$$

where the molecular weight of the mixture is given by

$$W = \left(\sum_i n_i\right)^{-1} \tag{50}$$

III. Comparison with the Blaze II Model

To develop a simplified cw chemical laser model that will give quantitative predictions, it is necessary to carry out as many detailed comparisons with other models or experimental data as possible. In the present study, two diverse cases were selected for initial baselining of the model. One is an arc-driven cw HF power spectral case[9] and the other is the CL XI lasing lines case.[10] In the interest of conciseness and because the CL XI was the more stringent test of the model (the higher temperature of the CL XI required a more extensive kinetics model), the results for that case will be presented here. It should be emphasized, however, that the quality of the results for the arc-driven laser are as good as the CL XI results.

In the diagnostic experiments with the CL XI nozzle, the power spectral distribution and the intensity distribution on each line were measured. The intensity distributions were measured with cylindrical mirrors oriented with the axis of the cylinder parallel to the x axis (flow direction). Thus, a Fabry-Perot model of the cavity should provide a good representation of this experiment.

The primary flow contained F, F_2, He, N_2, CF_4, and DF and the secondary flow contained H_2 and He. The N_2, CF_4, and DF were treated as inert species which were represented by argon in the present simplified model. To preserve numbers of particles, the total molar flow rate of these species was replaced by the same molar flow rate of argon. To verify the simplified kinetics model, the emphasis to date has been on comparing the present MNORO model run in the equilibrium mode with the Blaze II results for the CL XI case.

Several Blaze II runs were made for this study. The first one allowed all bands up to 8→7 to lase. The second case allowed only 3→2, 2→1, and 1→0 to lase. The last case allowed only 2→1 and 1→0, the bands observed experimentally, to lase. The Blaze II calculations took the effect of the nozzle trip flow on the mixing into account by increasing the binary diffusion coefficient. This multiplier was established by comparison of lasing zone length and total power with experimental data for the case when all bands up to 8→7 could lase if conditions would allow it. The results of these three runs are shown in Table 1. The effect of the change in the vibrational bands which were allowed to lase on the fluid dynamic and species profiles is shown in Figs. 3 and 4. From these figures, it is seen that the hot reaction bands have a negligible effect on these profiles. Not allowing lasing to occur on 3→2 results in a 10% increase in the peak pressure and temperature and a negligible effect on the other profiles except for the HF(3) profile. Thus, one set of fluid profiles was used throughout this study. The polynomials give an excellent representation of the fluid dynamic variables. The hot reaction bands have a negligible influence on the 2→1 power spectral distribution. However, lasing on 3→2 has a significant effect not only on the total power in the 2→1 band (Table 1), but also on the 2→1 power spectral distribution.

The MNORO results when the hot reaction (6) is included by pumping only to HF(3) and when multiquantum VT deactivation by HF, F, and H are included are shown in Figs. 5 and 6. Because of the relatively high temperature ($T_{max} = 585$ K) and the F-atom wall recombination which results in a significant amount of F_2, the hot pumping

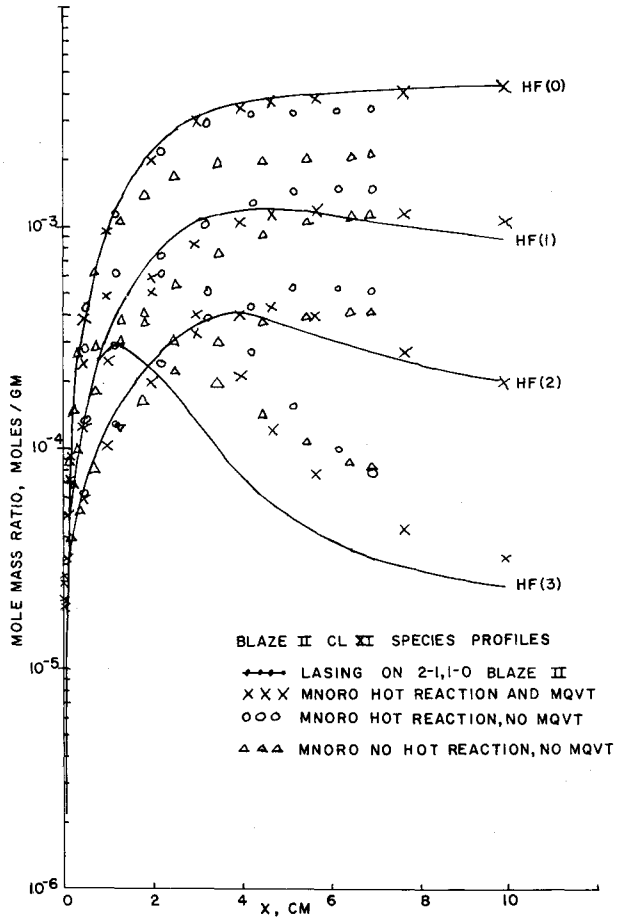

Fig. 6 Comparison of Blaze II and MNORO rotational equilibrium HF(v) profiles for the CL XI showing the effect of the hot reaction and MQVT.

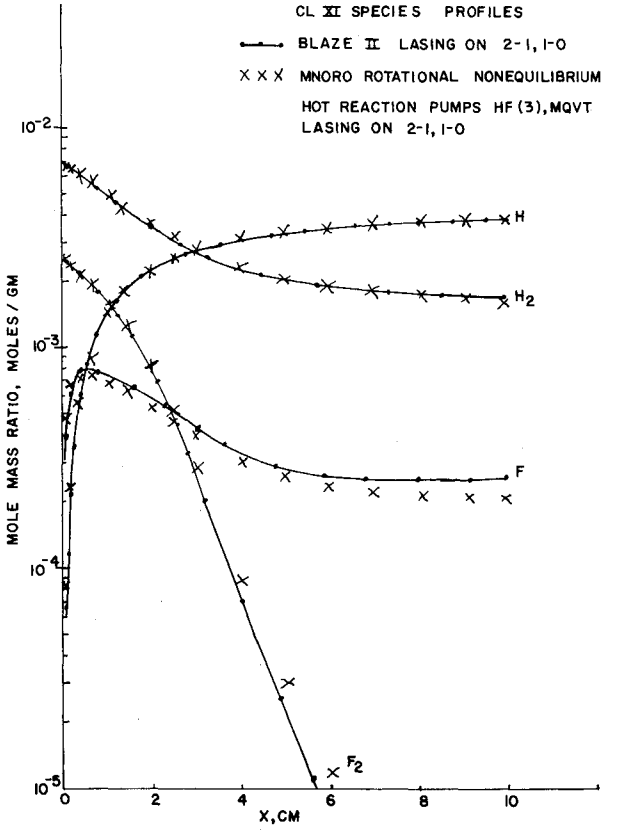

Fig. 7 Comparison of Blaze II and rotational nonequilibrium MNORO H, F, H_2, and F_2 profiles for CL XI.

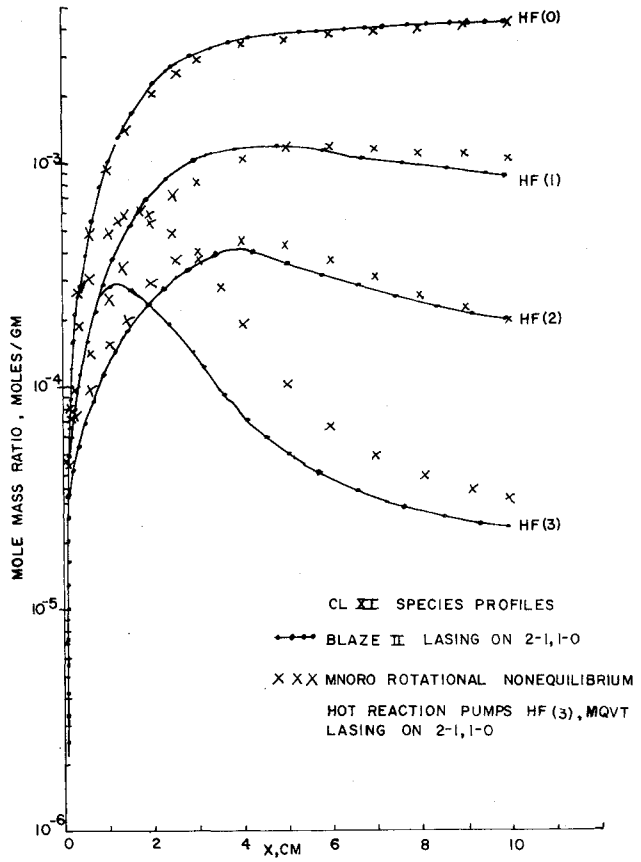

Fig. 8 Comparison of Blaze II and rotational nonequilibrium MNORO HF(v) profiles for CL XI.

reaction must be included in the kinetic model to duplicate the Blaze II F, H, and F_2 profiles (Fig. 5). As might be expected, the multiquantum deactivation has a negligible effect on the F, H, F_2, and H_2 species profiles. From Fig. 6 it is seen that both the hot reaction and multiquantum deactivation are required to obtain good agreement with the Blaze II HF(v) profiles. The agreement it not as good for HF(3) because the hot reaction is pumping completely to HF(3) rather than to the upper levels with collisional cascade to HF(3). When hot reaction pumping to HF(3) and HF(4), where

$$k^4_{PH} = \sum_{v=4}^{6} k^v_{PH}$$

is included, there is no change in the HF(v) species profiles for $v=0$, 1, 2, and only a slight improvement in HF(3). To obtain better agreement with HF(3) would require including at least up to HF(5) because, based on the magnitude of the rate constants involved, there is a bottleneck at HF(4) which would result in decreased HF(3). Since the effect on the 2→1 power and power spectral distribution would be small, the additional complexity is not warranted. Thus, the final model includes the effect of the hot reaction by allowing it to pump to HF(3) only, i.e.,

$$k^3_{PH} = \sum_{v=3}^{6} k^v_{PH}$$

From runs made with only the 2→0 multiquantum deactivation and with 2→0, 3→1, and 3→0, the most important of these reactions is the 2→0 deactivation by a factor of about 2:1.

The rotational nonequilibrium species profiles when the hot reaction pumps only to HF(3) and multiquantum deactivations are included are compared to the Blaze II profiles in Figs. 7 and 8. As can be seen, the nonequilibrium species

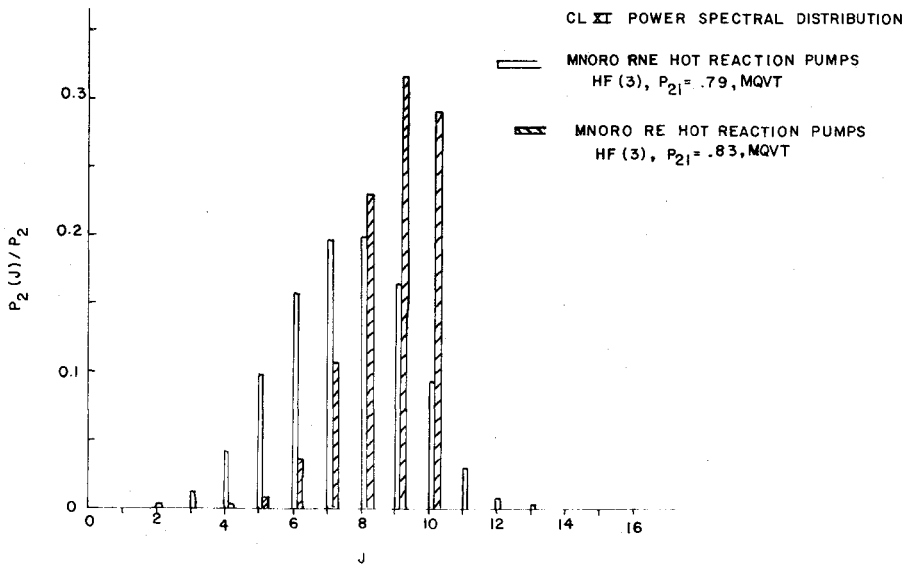

Fig. 9 Comparison of rotational equilibrium (RE) and rotational nonequilibrium (RNE) MNORO power spectral distributions.

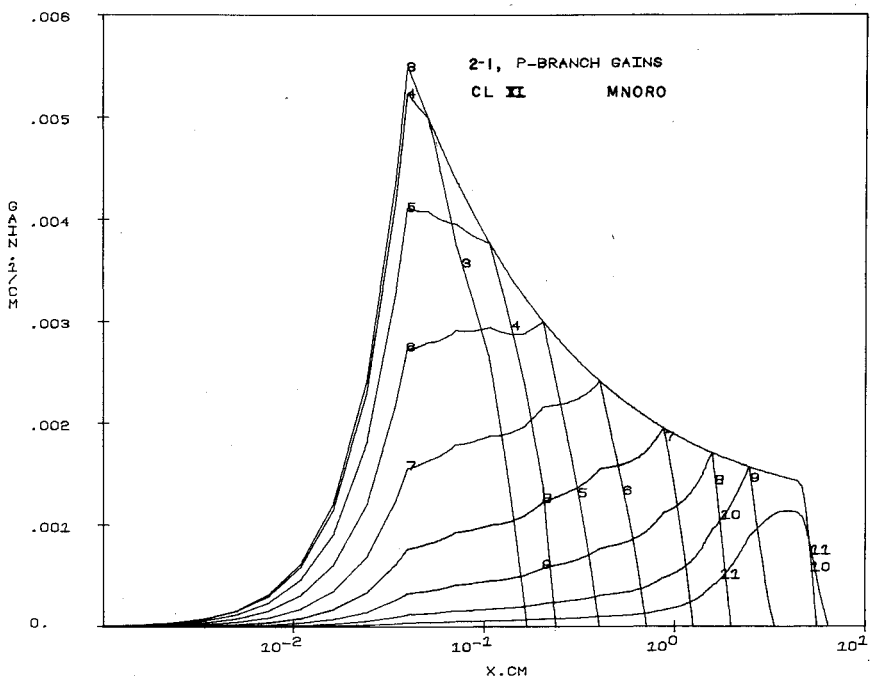

Fig. 10 MNORO rotational equilibrium *P* branch saturated gains for CL XI.

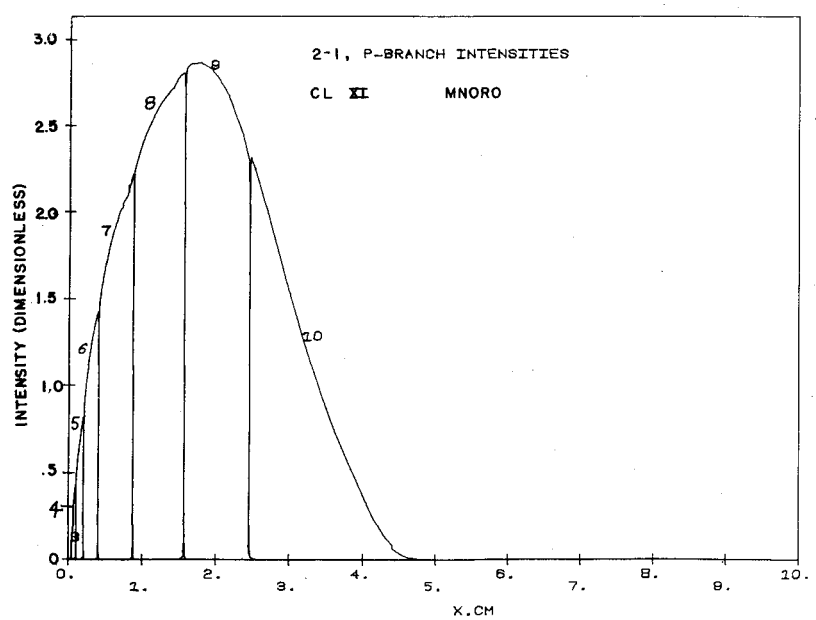

Fig. 11 MNORO rotational equilibrium *P* branch intensity distributions for CL XI.

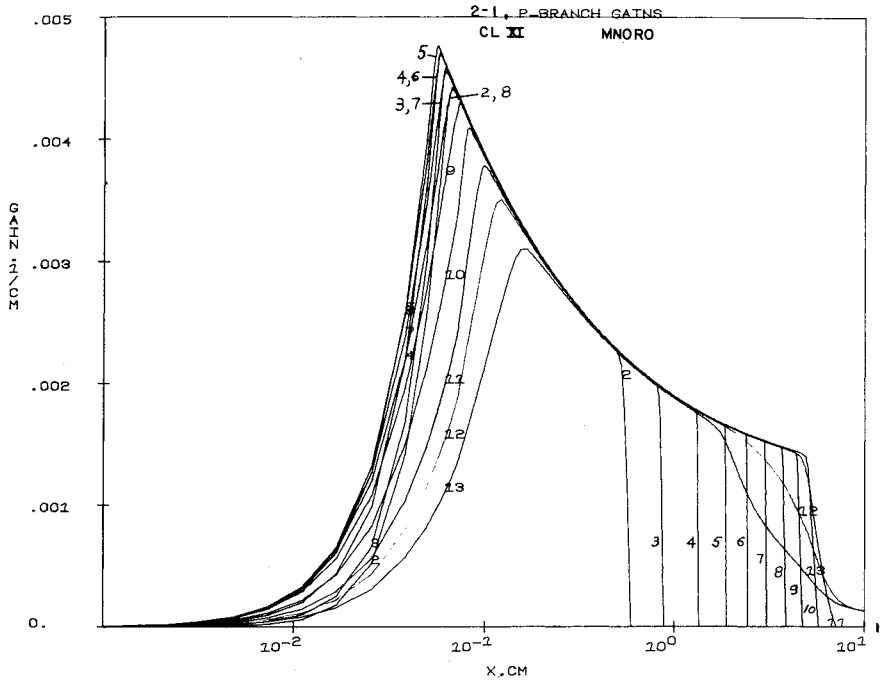

Fig. 12 MNORO rotational nonequilibrium P branch saturated gains for CL XI.

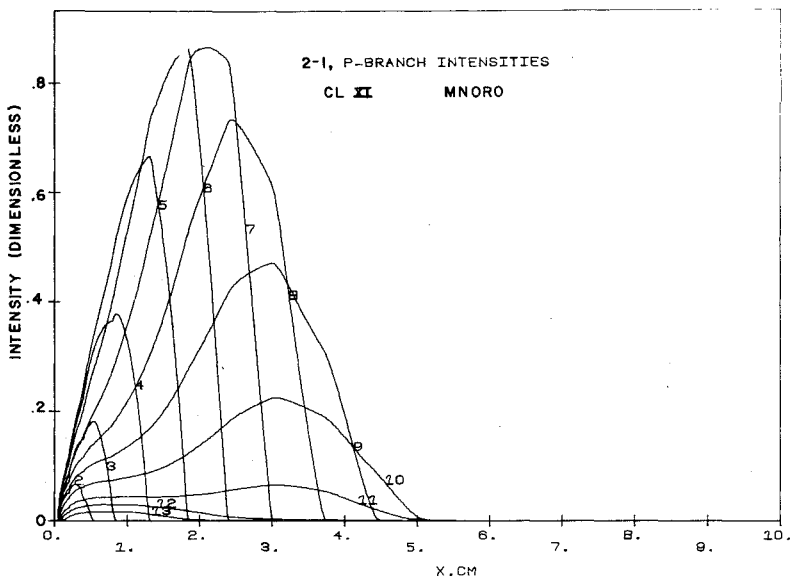

Fig. 13 MNORO rotational nonequilibrium P branch intensity distributions for CL XI.

profiles agree as well with the Blaze II species profiles as the equilibrium ones do. However, it is seen from Fig. 9 that the nonequilibrium power spectral distribution is considerably different than the equilibrium power spectral distribution (PSD). The peak of the nonequilibrium PSD at $J=8$ is indicative of the relatively large $T(T_{\max}=585$ K); since the experimental data peaks at $J=6$, Blaze II may be overpredicting the temperature.

Figures 10-13 give the rotational equilibrium and the rotational nonequilibrium saturated gains and intensity distributions. The J-shifting is evident in the gain and intensity distributions for the equilibrium case, whereas simultaneous lasing on many lines occurs in the nonequilibrium case.

From the Blaze II results (Table 1), it is seen that the occurrence of lasing on $3\rightarrow2$ results in a 21% increase in the power on $2\rightarrow1$; MNORO indicates a 24% increase when lasing on $3\rightarrow2$ occurs (lasing on $3\rightarrow2$ is simulated in MNORO by setting $k_p^2=k_p^2+k_p^3$). Since this is a significant effect which was also found in the arc-driven laser case, it may be worthwhile promoting $3\rightarrow2$ lasing to obtain the increased performance on $2\rightarrow1$ and $1\rightarrow0$. It should be noted that the equilibrium and the nonequilibrium powers only differ by about 4% rather than the 20% difference[1] observed in premixed cases.

From these comparisons, it is seen that the MNORO model includes the essential elements required to give good agreement with the very detailed Blaze II model. These elements are, in addition to the pumping, collisional deactivation and rotational relaxation reactions, lasing on $1\rightarrow0$ and $3\rightarrow2$ if it occurs, F-atom wall recombination, and the hot reaction. The importance of the multiquantum deactivation depends upon the temperature. For low temperatures ($\sim$300 K), multiquantum effects were less than 3%; however, for the CL XI device in which the temperature was quite high ($\sim$585 K), multiquantum deactivation results in about a 29% decrease in power and has a significant effect on the length of the lasing zone (Table 2).

In Fig. 14, the MNORO rotational nonequilibrium power spectral distributions are compared to experimental data for the CL XI and for the arc-driven laser. The agreement is quite good for the arc-driven laser; as pointed out previously, the peak in the CL XI theoretical power spectral distribution at $J=8$ is due to the high temperature predicted by Blaze II. The

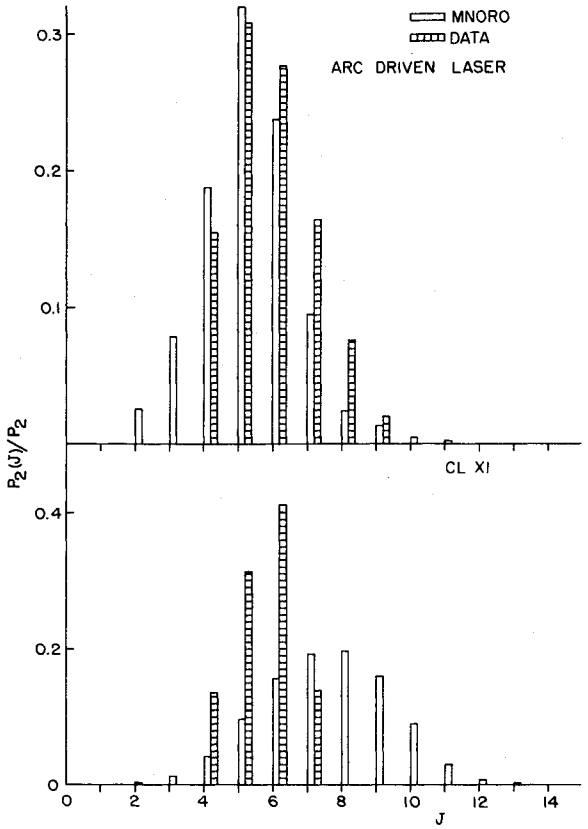

Fig. 14 Comparison of experimental and MNORO rotational nonequilibrium power spectral distributions (data are from Refs. 9 and 10).

Table 2 Effect of hot reaction and multiquantum VT deactivation on the 2→1 power and the length of the lasing zone for CL XI

Model	P_{21}	X_{cutoff}
Blaze II	1.0	1.0
MNORO		
NO hot reaction	0.89	1.87
NO MQVT		
Hot reaction	1.27	1.57
NO MQVT		
Hot reaction	0.98	1.15
MQVT		
Rotational		
Nonequilibrium	0.93	1.25
Hot reaction		
MQVT		

greater number of lasing lines predicted by the model may be due to the fact that the experimental CL XI resonator was not a Fabry-Perot cavity, whereas the data of Ref. 9 was obtained with a Fabry-Perot resonator.

The rotational nonequilibrium model employs sparse matrix techniques in the evaluation and inversion of the Jacobian matrix used by the implicit integration scheme. The use of sparse matrix techniques reduces run time by a factor of three. The MNORO model varied from 108 s for the arc-driven laser case to 248 s for the CL XI case (all times are on the CYBER 175). This difference in run time is the result of the different pressures in the two cases. The CL XI pressure is in the range of 15-20 Torr, while the arc-driven laser pressure is 1.4 Torr. When the CL XI is run with the pressure reduced by a factor of 10, the execution time is 66 s, and when the arc-driven laser is run with the pressure increased by a factor of 10, the run time is 203 s. It should be noted that variation in other parameters such as the temperature profile, mass flow rates, and mirror reflectivities had at most a 10% effect on run time.

The physical reason the pressure has such an effect is that the kinetic terms depend upon ρ^2 and hence P^2; thus, a factor of 10 in the pressure changes the magnitude of the kinetic terms by a factor of 100, which significantly influences the stiffness of the equation system. This is manifested in the gain curves; the high-pressure case reaches saturation at a one order of magnitude smaller value of x than the low-pressure case.

IV. Concluding Remarks

From the detailed comparison between the Blaze II and MNORO results, the objective of developing an efficient rotational nonequilibrium model of a cw chemical laser which is capable of giving quantitative predictions of the power spectral distribution has been achieved. The essential elements required for a quantitative, rotational nonequilibrium model have been identified. In addition, the prediction by the very complete laser models[6-8] of lasing on the upper vibrational bands and on 3→2 for cases in which the experimental data indicate no lasing above 2→1 suggests a fundamental problem with the HF rate package, either in the pumping rates to the higher vibrational levels or in the deactivation rates of those higher levels.

References

[1] Sentman, L. H., "Rotational Nonequilibrium in cw Chemical Lasers," *Journal of Chemical Physics*, Vol. 62, May 1975, pp. 3523-3537.

[2] Hough, J.J.T. and Kerber, R. L., "Effect of Cavity Transients and Rotational Relaxation on the Performance of Pulsed HF Chemical Lasers: A Theoretical Investigation," *Applied Optics*, Vol. 14, Dec. 1975, pp. 2960-2970.

[3] Hall, R. J., "Rotational Nonequilibrium and Line-Selected Operation in cw DF Chemical Lasers," *IEEE Journal of Quantum Electronics*, Vol. QE-12, Aug. 1976, pp. 453-462.

[4] Skifstad, J. G. and Chao, C. M., "Rotational Relaxation in a Line-Selected Continuous HF Chemical Laser," *Applied Optics*, Vol. 14, July 1975, pp. 1713-1718.

[5] Sentman, L. H., "Chemical Laser Power Spectral Performance: A Coupled Fluid Dynamic, Kinetic and Physical Optics Model," *Applied Optics*, Vol. 17, July 1978, pp. 2244-2249.

[6] Sentman, L. H., Subbiah, M., and Zelazny, S. W., "Blaze II: A Chemical Laser Simulation Computer Program," Bell Aerospace Textron, Buffalo, New York, T.R. H-CR-77-8, Feb. 1977 (prepared for U.S. Army Missile Research and Development Command, Redstone Arsenal).

[7] Thoenes, J., McDanal, A. J., Ratliff, A. W., and Smith, S. D., "Analysis of Chemical Lasers," Lockheed Missiles and Space Co., Inc., Huntsville, Ala., Lockheed Tech. Rept. RK-CR-74-13, Vols. 1-5, June 1974.

[8] Ramshaw, J. D. and Dukowicz, J. K., "APACHE: A Generalized-Mesh Eulerian Computer Code for Multicomponent Chemically Reactive Fluid Flow," Los Alamos Scientific Lab., LA-7427, Jan. 1979.

[9] Spencer, D. J., Mirels, H., and Durran, D. A., "Performance of cw HF Chemical Laser with N_2 or He Diluent," The Aerospace Corp., Los Angeles, Calif., TR-01722(2777)-1, March 1972.

[10] Tregay, G. and Driscoll, R. J., Bell Aerospace Textron, private communication, Oct. 1978.

[11] Sentman, L. H. and Brandkamp, W., "An Efficient Rotational Nonequilibrium Model of a cw Chemical Laser," Aeronautical and Astronautical Engineering Dept., University of Illinois, Urbana, Ill., TR 79-5, July 1979.

[12] Polanyi, J. C. and Woodall, K. B., "Energy Distribution Among Reaction Products, VI. $F+H_2$, D_2," *Journal of Chemical Physics*, Vol. 57, Aug. 1972, pp. 1574-1586.

[13] Polanyi, J. C. and Woodall, K. B., "Mechanism of Rotational Relaxation," *Journal of Chemical Physics*, Vol. 56, Feb. 1972, pp. 1563-1572.

[14] Hinchen, J. J., "Rotational Population Transfer in HF," *Applied Physics Letters*, Vol. 27, Dec. 1975, pp. 672-673.

[15] Sentman, L. H., "Rotational Relaxation of HF," *Journal of Chemical Physics*, Vol. 67, Aug. 1977, pp. 966-969.

[16] Emanuel, G., "Numerical Modeling of Chemical Lasers," *Handbook of Chemical Lasers*, edited by R.W.F. Gross and J. F. Bott, John Wiley & Sons, New York, 1976, pp. 469-549.